Examining Relationships between Environmental Conditions and Supercell Motion in Time

MATTHEW D. FLOURNOY,[a] MICHAEL C. CONIGLIO,[b] AND ERIK N. RASMUSSEN[a]

[a] *Cooperative Institute for Mesoscale Meteorological Studies, Norman, Oklahoma*
[b] *NOAA/National Severe Storms Laboratory, School of Meteorology, University of Oklahoma, Norman, Oklahoma*

ABSTRACT: Although environmental controls on bulk supercell potential and hazards have been studied extensively, relationships between environmental conditions and temporal changes to storm morphology remain less explored. These relationships are examined in this study using a compilation of sounding data collected during field campaigns from 1994 to 2019 in the vicinity of 216 supercells. Environmental parameters are calculated from the soundings and related to storm-track characteristics like initial cell motion and the time of the right turn (i.e., the time elapsed between the cell initiation and the first time when the supercell obtains a quasi-steady motion that is directed clockwise from its initial motion.). We do not find any significant associations between environmental parameters and the time of the right turn. Somewhat surprisingly, no relationship is found between storm-relative environmental helicity and the time elapsed between cell initiation and the onset of deviant motion. Initial cell motion is best approximated by the direction of the 0–6-km mean wind at two-thirds the speed. This is a result of advection and propagation in the 0–4- and 0–2-km layers, respectively. Unsurprisingly, Bunkers-right storm motion is a good estimate of post-turn motion, but storms that exhibit a post-turn motion left of Bunkers-right are less likely to be tornadic. These findings are relevant for real-time forecasting efforts in predicting the path and tornado potential of supercells up to hours in advance.

SIGNIFICANCE STATEMENT: Most of the strongest and deadliest tornadoes are produced by a type of thunderstorm called a ''supercell.'' Forecasters use many tools to help diagnose which environments favor supercells and which do not. However, given conditions favorable for supercells, we do not know much about how the supercell will evolve in time. This study identifies relationships (or the lack thereof) between background conditions and developing supercells, particularly related to storm path. Surprisingly, despite well-established relationships between supercell characteristics and the environment, we do not find any significant relationships between environmental parameters and changes in the supercells' paths early in their life cycles. These findings are relevant for forecasters tasked with predicting supercell paths up to hours in advance.

KEYWORDS: Convective storms/systems; Convective-scale processes; Supercells; Tornadoes; Storm environments

1. Introduction

a. Environmental influences on supercell potential

The evolution of a supercell thunderstorm and associated severe hazards are strongly related to the background environment within which the storm forms. Given discrete convection initiation, supercell formation is generally expected if the background environment contains sufficient convective available potential energy (CAPE $\geq 1000\,\mathrm{J\,kg^{-1}}$), vertical wind shear (0–6 km AGL shear ≥ 15–$20\,\mathrm{m\,s^{-1}}$), and 0–3-km storm-relative helicity (SRH $\geq 100\,\mathrm{m^2\,s^{-2}}$). These general thresholds (not met stringently in all cases) have been found in multiple studies analyzing soundings in the vicinity of supercells (e.g., Rasmussen and Blanchard 1998; Thompson et al. 2003; Craven and Brooks 2004). These studies also noted additional differences between environments supporting supercells and those supporting ordinary cells or marginal supercells, including lower lifted condensation levels (LCLs), greater 0–1-km shear magnitudes and upper-tropospheric storm-relative flow, and larger 0–3-km CAPE in supercell environments. These

parameters and others derived from them (like the supercell composite parameter, energy helicity index, etc.) are used to predict supercell potential days in advance, as well as supercell evolution once a storm has formed.

The physical processes driving these relationships have been well explored. Numerous theoretical and numerical studies have shown that increased SRH is associated with greater streamwise horizontal vorticity that, when acted upon by an updraft, is tilted into the vertical to form the midlevel mesocyclone (e.g., Lilly 1982, 1986; Weisman and Klemp 1982; Davies-Jones 1984). In addition to the magnitude of streamwise horizontal vorticity, SRH is also modified by storm-relative wind speed; to this end, greater storm-relative wind speeds have been shown to increasingly favor supercell development (e.g., Droegemeier et al. 1993; Thompson et al. 2003; Peters et al. 2019, 2020). In particular, numerical simulations suggest that stronger storm-relative wind supports wider updrafts that are more resistant to dilution and its deleterious effect on buoyant accelerations driven by CAPE (Peters et al. 2019, 2020). Finally, lower LCLs are associated with greater boundary layer relative humidity; given a similar mid- to upper-tropospheric thermodynamic profile, these yield greater CAPE and a deeper effective storm-inflow layer, along with an environment that limits the coldness in the outflow that

can disrupt storm organization. These processes contribute to a stronger, deeper updraft closer to the surface more capable of modifying environmental wind shear to acquire supercellular characteristics.

For obvious reasons, many studies of modeled or observed supercell proximity soundings have focused on differences between tornadic and nontornadic environments. The general consensus is that supercellular tornado potential is largely influenced by boundary layer humidity and low-level shear. This finding is consistent across multiple observational (e.g., Rasmussen and Blanchard 1998; Rasmussen 2003; Thompson et al. 2003; Craven and Brooks 2004; Parker 2014; Wade et al. 2018; Coniglio and Parker 2020, hereafter CP20) and modeling (e.g., Markowski and Richardson 2014; Coffer and Parker 2017) studies, especially when differentiating between nontornadic and significantly tornadic (EF2 or greater) supercells.

b. Environmental influences on supercell morphology

Less work has focused on the influence of the environment on temporal changes in supercell behavior. One defining characteristic of supercells is their longevity, and while by definition they primarily contain a single dominant, quasi-steady updraft during their entire lifespan (Glickman 2000), changes in storm intensity, motion, and morphology occur. A few studies have examined how changes in the background environment influence changes in supercell behavior. Richardson et al. (2007) used an idealized framework to examine the influence of horizontally varying environmental vertical shear on updraft development and found that multicell systems intensified into more organized, bow echo structures when the entire storm system moved into increasing shear. Ziegler et al. (2010) used a similar approach to simulate supercell evolution moving from a weakly capped region into a cold boundary layer and inversion region. Some studies have used the base-state substitution technique of Letkewicz et al. (2013) to examine how temporal changes in the background environment influence a mature supercell (Coffer and Parker 2015; Davenport and Parker 2015; Davenport et al. 2019). Others have analyzed observations in the vicinity of intensifying or dissipating supercells and attributed these evolutionary paths, including tornado production (Klees et al. 2016), to changes in environmental SRH, convective inhibition, and vertical wind profiles (Davenport and Parker 2015; Gropp and Davenport 2018).

This study has a similar goal of relating supercell behavior to environmental characteristics except we specifically focus on the motion of the supercell during the first 1–2 h after initiation. In particular, we focus on storm motion as a function of time given a constant background environment. If storm motion is only influenced by advection, it should align with the mean wind in the layer of the atmosphere that the storm occupies. However, numerous studies have documented the tendency for "large and intense" (Browning 1964) cells to move to the right of the mean wind (e.g., Newton and Katz 1958), even early in their lifetime (e.g., Rotunno and Klemp 1982). This is due to small-scale pressure perturbations that form in the vicinity of the cell, which under the Boussinesq approximation (i.e., shallow flows) can be expressed as

$$p' \propto (e'_{ij})^2 - \frac{1}{2}|\boldsymbol{\omega}'|^2 + 2\left(\frac{\partial w'}{\partial x}\frac{\partial \overline{u}}{\partial z} + \frac{\partial w'}{\partial y}\frac{\partial \overline{v}}{\partial z}\right) - \frac{\partial B}{\partial z}. \quad (1)$$

In Eq. (1) (Markowski and Richardson 2010), B is the buoyancy, $\overline{u}$ and $\overline{v}$ are the horizontal, base-state wind components, w' is the vertical velocity ($\overline{w} = 0$), $\boldsymbol{\omega}'$ is the perturbation vorticity, and e'_{ij} is the rate-of-strain tensor for the perturbation winds (also called the deformation tensor), which is expressed as

$$(e'_{ij})^2 = \frac{1}{4}\sum_{i=1}^{3}\sum_{j=1}^{3}\left(\frac{\partial u'_i}{\partial x_j} + \frac{\partial u'_j}{\partial x_i}\right)^2. \quad (2)$$

The first two terms on the right-hand side of Eq. (1) represent nonlinear, dynamic perturbations (p'_{NL}), the third represents linear, dynamic perturbations (p'_L), and the last represents buoyant perturbations (p'_B). The sum of p'_{NL} and p'_L represents the total dynamic pressure perturbation contribution (p'_D). This decomposition of p' is summarized below as

$$p' = p'_D + p'_B = p'_{NL} + p'_L + p'_B. \quad (3)$$

Some studies have examined the relative influences of p'_{NL} and p'_L on developing supercell motion. In environments with a straight hodograph, p'_L (the so-called updraft-in-shear effect) results in cell propagation downshear (Rotunno and Klemp 1982); this scenario yields a storm motion with components along the mean wind (due to advection) and along the shear vector (due to propagation). In environments with a clockwise-curving hodograph, p'_L results in both propagation downshear as well as propagation to the right of the mean shear vector (Rotunno and Klemp 1982, 1985). This yields a storm motion further to the right of the mean wind than in the straight-hodograph case (see Fig. 3 of Rotunno and Klemp 1982). Finally, p'_{NL} influences storm motion by enhancing both the right and left flanks of the initial updraft. The combination of linear and nonlinear effects (to some degree) leads to storm-splitting (Rotunno and Klemp 1982, 1985; Weisman and Klemp 1982, 1984), although Davies-Jones (2002) showed that p'_{NL} results in the splitting midlevel vortices propagating into regions of downdraft rather than updraft, and thus questioned its influence on updraft motion. Regardless, the effects of p'_L become more dominant as hodograph curvature increases (Weisman and Rotunno 2000; Davies-Jones 2002). Numerous studies have examined the motion of supercells after this developmental phase (i.e., "post-turn") and related it to environmental conditions (Maddox 1976; Davies and Johns 1993; Rasmussen and Blanchard 1998). Bunkers et al. (2000) developed a hodograph technique that exploits the above relationships between deviant supercell motion and the environmental shear that is Galilean invariant and therefore is applicable to a wide variety of flow scenarios (Bunkers 2018). This method is used widely to help anticipate the eventual mature supercell motion and is used to calculate environmental parameters (like SRH) that depend on storm motion.

Processes influencing the deviant motion of developing supercells may occur very quickly as interactions between the storm-scale updraft and background vertical wind shear result in horizontal pressure perturbation gradients across the cell.

Rotunno and Klemp (1982) showed that both p'_L and p'_{NL} influenced cell motion within the first 15 min in environments with veering vertical wind shear. They found nonlinear forcing to favor storm splitting and the linear forcing to preferentially favor the right flank, resulting in an "early rightward bias" with respect to the shear and mean wind. In the case of a straight hodograph, cell splitting was attributed solely to p'_{NL}. In the aforementioned studies, cell splitting was generally noted 20–60 min into each simulation (Rotunno and Klemp 1985; Weisman and Klemp 1982, 1984). In a revisitation of these topics, Weisman and Rotunno (2000) found that initial simulated cells tended to move generally in the direction of, but slower than, the 0–6-km mean wind during the first 40 min (see their Fig. 4). By 80 min, all cases moved significantly rightward with respect to the mean wind, "consistent with the development of rotational updraft after 40 minutes." Cai and Wakimoto (2001) examined retrieved pressure fields in the vicinity of an observed supercell and found that, although the storm formed in an environment characterized by a straight hodograph, p'_L was more important than p'_{NL} in governing the rightward deviance of the cell at earlier times (although it is unclear how long after initial convection initiation this analysis was first performed).

Some analysis by Bluestein and Parker (1993) partially addressed observed cell motion and environmental characteristics during the developmental phase of supercells. They analyzed WSR-57 microfilm data from 61 supercells occurring from 1971 to 1986 to define modes of isolated, severe convection initiating along the dryline in the southern Great Plains. Part of their work documented the mean wind (obtained from a variety of standard radiosonde observations, special soundings during field experiments, and regional surface and upper-air maps), initial cell motion during the first 30 min after the first radar echo, and later cell motion in a 40-min window centered on the time of the first occurrence of severe weather. Figure 1 shows these results grouped by development types (see Fig. 1 in Bluestein and Parker 1993), revealing that in all cases the initial cell motion was significantly slower than the 0–6 km AGL pressure-weighted mean wind but generally aligned in the same direction. This is consistent with the findings of Weisman and Rotunno (2000).

These findings leave unanswered questions regarding storm motion during supercell development, including:

- How long does it take a developing supercell to turn right? How is this time scale influenced by environmental characteristics?
- Is the initial cell motion (prior to the right turn) generally aligned with the mean wind or shear in different layers?
- Are the answers to the above questions different for supercells destined to be tornadic verses those that remain nontornadic?

This study explores these questions using data from a compilation of hundreds of soundings collected during past field experiments (CP20). These data have greater temporal and vertical resolution than traditional sounding data, thus offering increased precision of environmental parameters in important regions of the atmosphere like the boundary layer. These findings lend insight into physical processes governing these relationships and will complement experimental products like

the NSSL Warn-on-Forecast System (Stensrud et al. 2009; Lawson et al. 2018) to better predict supercell motion in real-time operations.

2. Data and methods

The source of data used here is the compilation of soundings presented in CP20, which synthesized data from 902 soundings collected during 13 field campaigns from 1994 to 2019 in the vicinity of 216 supercells. The data were extensively quality controlled (objectively and manually), and the native 1–2-Hz observations were interpolated to a vertical grid spacing of 10 m, yielding much greater vertical resolution than traditional radiosonde data. CP20 used this novel dataset to assess relationships between the background environment and supercellular tornado potential as well as environmental heterogeneities present in the inflow region of supercells. In the present study, the soundings that are deemed to be representative of the storm environment (described later) are used to relate the environment to supercell evolution focusing on the relationships between sounding variables and storm motion at the time of the sounding. Interested readers are referred to CP20 for more information about the construction of this sounding dataset.

This study also makes use of storm-track data compiled by CP20. WSR-88D level II data were manually scrutinized for each case to ensure that supercell characteristics (e.g., a hook echo, bounded weak echo region, or mesocyclone) persisted for at least 60 min. Meeting that criterion, the latitude and longitude of the supercell updraft, demarcated by the low-level, weak-reflectivity notch downshear of the hook echo, were manually recorded using the NCEI Weather and Climate Toolkit at every volume time (around every 5.5 min) from the first echo to when the supercell dissipated or merged with other storms and/or could not be identified. The motion of each supercell at each volume time was determined using a five-point (20–25 min) weighted average of instantaneous storm-motion components (using weights of 0.05, 0.2, 0.5, 0.2, and 0.05). The instantaneous storm motions were based on the bearing and great circle distance between successive latitude–longitude points assigned to the storm. Having these estimates at high temporal resolution through the storm life cycle provides an opportunity to examine changes in motion at finer detail than presented in past studies. Finally, tornado occurrence or lack thereof was noted at every volume time based on Storm Prediction Center Severe Weather Database files and NWS Storm Data. For more information on these procedures, see CP20.

The present study uses the above storm-track information compiled from 220[1] supercells. A key focus of this study involves the time elapsed between the first echo and the right turn of the storm, i.e., the time elapsed between the cell

---

[1] Four additional supercells were tracked with no radiosonde data in their vicinity. Thus, 216 supercells were analyzed when relating supercell track characteristics to environmental parameters, and 220 supercells were analyzed when examining supercell track characteristics alone.
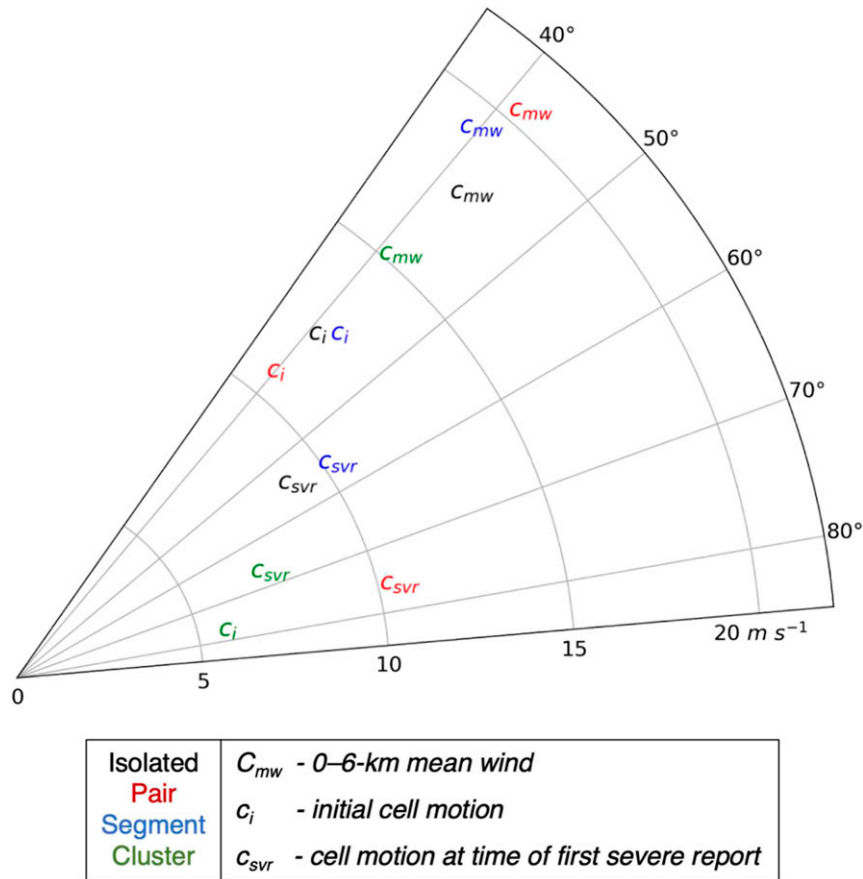
FIG. 1. Observed supercell storm motions documented by Bluestein and Parker (1993). Subscripts indicate storm motion derived from the 0–6 km AGL pressure-weighted mean wind from the closest sounding and surface observations (c_{mw}), observed radar-derived storm motion during the first 30 min after the echo appeared (c_i), and observed storm motion averaged over a 40-min window centered on the time of the first occurrence of severe weather (c_{svr}). Each motion is plotted according to its speed (m s^{-1}) and bearing (°). Colors indicate the type of supercellular development (see Fig. 1 of Bluestein and Parker 1993); black represents isolated cases ($n = 37$), red represents pair cases ($n = 6$), blue represents line segment cases ($n = 8$), and green represents cluster cases ($n = 5$). All of these development types resulted in one discrete cell around 30 min after the initial radar echoes appeared.

initiation (i.e., generally when 35 dBZ appeared on the lowest available tilt) and the first time when the supercell obtains a quasi-steady motion that is directed clockwise from its initial motion. Left-moving supercells are not included in this study because right movers have been the primary focus of data collection during past field campaigns. Given the sample size and different storm motions within this entire sample, a subjective method based solely on the storm track (i.e., not including environmental information) was used to determine the time at which each storm turned right. This time for each storm was determined independently by each coauthor. Of the 220 storms, we agreed exactly on the time of the right turn (or the lack of a right turn) in nearly one-third of the sample ($n = 71$). In 60% of storms ($n = 133$), we either all identified no right turn or identified the same right-turn period but were separated in time by no more than 15 min (including the 71 storms mentioned

above). Of the remaining 87 storms, at least one of us failed to agree with the others on either the occurrence of a right turn or the specific time of a right turn (within 15 min of the other coauthors).[2] Because of this, the analysis presented in this paper was performed four times. Three used the right-turn times identified by each coauthor and a fourth used the right-turn times identified by the first author with 44 storms removed due to large disagreements (>15 min) between coauthors regarding the time of the right turn. The results do not qualitatively differ across these experiments. Quantitative results differ slightly and are mentioned in the text when they either impact statistical significance or are deemed relevant for operational

---

[2] Plots of each storm's track and time of the right turn from each coauthor are available in the GitHub repository noted in the data availability statement.

TABLE 1. General characteristics of all storms ($n = 169$) as well as the tornadic ($n = 90$) and nontornadic ($n = 79$) subsets identified using the right-turn times selected by the first author. Storm motions include the storm speed (m s^{-1}) followed by the storm direction (degrees). The storm motions are presented in a coordinate system with the initial storm motion along 270° to ease the comparison to the pre- and post-turn directions. The initial storm motion is the mean motion during the first 20 min of the storm track. The pre- and post-turn motions are the mean motions during the 15–35-min period before and after the time of the right turn, respectively. The final column shows the differences between the pre- and post-turn speed and direction.

	Time of the right turn (min)				Storm motion (m s^{-1}/degrees)			
	Mean	Std dev	Min	Max	Initial	Pre-turn	Post-turn	Difference
All storms (169)	43.8	28.3	10.0	190.0	12.9/270.0	12.9/271.3	12.5/295.3	−0.49/24.0
Tornadic (90)	43.9	30.7	10.0	190.0	13.5/270.0	13.5/271.5	13.0/294.9	−0.54/23.4
Nontornadic (79)	43.7	25.2	10.0	145.0	12.2/270.0	12.3/270.9	11.9/295.8	−0.41/24.9

purposes. Of the 220 supercells in the dataset, the first author found 169 to exhibit clear right turns during their lifespan. The analysis presented here is derived from these right-turn times.

While it did not influence the findings of this study, it is interesting that such a range of right-turn identifications existed between the three coauthors. Many of the discrepancies were small, and our right-turn times still fell within the same general right-turn period. Others did not and involved inflections along the storm track that one or two of us believed was a right turn while the other(s) did not. A somewhat consistent signal was for these disagreements to occur when an inflection in the storm path was present in the first 10–20 min of the storm's lifetime. A goal of a future study is identifying under what conditions these "early turns" occur and the processes responsible for them.

Multiple sounding parameters are evaluated in this study and related to the supercell right turn. These parameters were selected because of their hypothetical relation to the time of the right turn as well as their prevalence in operational forecasting. Thermodynamic variables like surface-based (SB) and mixed-layer (ML; calculated in the lowest 100 hPa) CAPE and convective inhibition (CIN) are analyzed due to their influences on updraft strength (and thus their indirect influences on p'_D). The 0–3-km SBCAPE is included because of its possible control on low-level updraft strength and the development of the low-level mesocyclone. MLLCL is analyzed due to its control on the updraft base[3] and strength as well as possible relationships to cold pool properties and subsequent influences on cell motion (e.g., Markowski et al. 2002). We hypothesize that stronger relationships between environmental parameters and the time of the right turn will occur with kinematic variables like mean storm-relative wind speed and streamwise/crosswise horizontal vorticity components in various layers. This is because of their controls on multiple storm-scale characteristics relevant to p'_D like updraft strength, width, rotational velocity, and inflow depth (e.g., Davies-Jones 1984; Peters et al. 2019, 2020).

Not every sounding from the CP20 dataset allows for computation of these variables. In general, sounding data are not used if 1) there are no data below 3 km AGL or 2) data are not available within 100 m of the top of a specified layer (e.g., no data within 2900–3100 m AGL when calculating mean storm-relative wind speed in the 0–3 km AGL layer). Soundings analyzed here are also restricted to the inflow sector. The definition of the storm inflow from CP20 is maintained here, namely that the sounding must have been launched outside of storm outflow within 120 km of the storm along an azimuth between −130° and 40° with respect to storm motion (see Fig. 5 of CP20) and contained 0–3-km SBCAPE > 0 J kg^{-1}. To maintain sampling independence for determination of statistical significance of differences in sounding subsets, only the first available sounding is selected for cases in which more than one sounding was launched on a storm (randomly changing which sounding is selected does not qualitatively change the results). The data are presented in the next section and are separated into two subsets, tornadic and nontornadic. The sounding parameter is considered "tornadic" if it was launched in the vicinity of a supercell that produced a tornado at any point during its life cycle.[4] The number of soundings plotted in each subset is displayed in each figure.

3. Results

a. Characteristics of the right turn

General characteristics of the right turn for the collection of 169 supercells are shown in Table 1. Across all storms, the mean time of the right turn after convection initiation was 43.8 min with a standard deviation of 28.3 min. The range of the time of the right turn across all storms was 10–190 min. Based on Monte Carlo testing, these values did not differ significantly between tornadic and nontornadic supercells.[5] Mean storm motions (defined as the direction the storm is coming from)

---

[3] Although the updraft base is controlled by the level of free convection (LFC), a higher or lower LFC is often associated with a higher or lower LCL, respectively. Thus, for example, lower LCLs often occur in conjunction with lower LFCs, implying lower updraft bases.

[4] This differs from the definition of "tornadic" used by CP20. In their study, a sounding was deemed "tornadic" if a tornado occurred any time within 6 min prior to and 90 min after the sonde was launched. Applying this definition in our case, focusing only on the earliest soundings launched near each storm, limits the tornadic sample size and is problematic for statistical comparison between tornadic and nontornadic cases.

[5] For the remainder of the paper, the difference of two means or medians is considered insignificant if the p value obtained from a two-tailed Monte Carlo test is between 0.05 and 0.95 (i.e., not significant at the 90% confidence level).
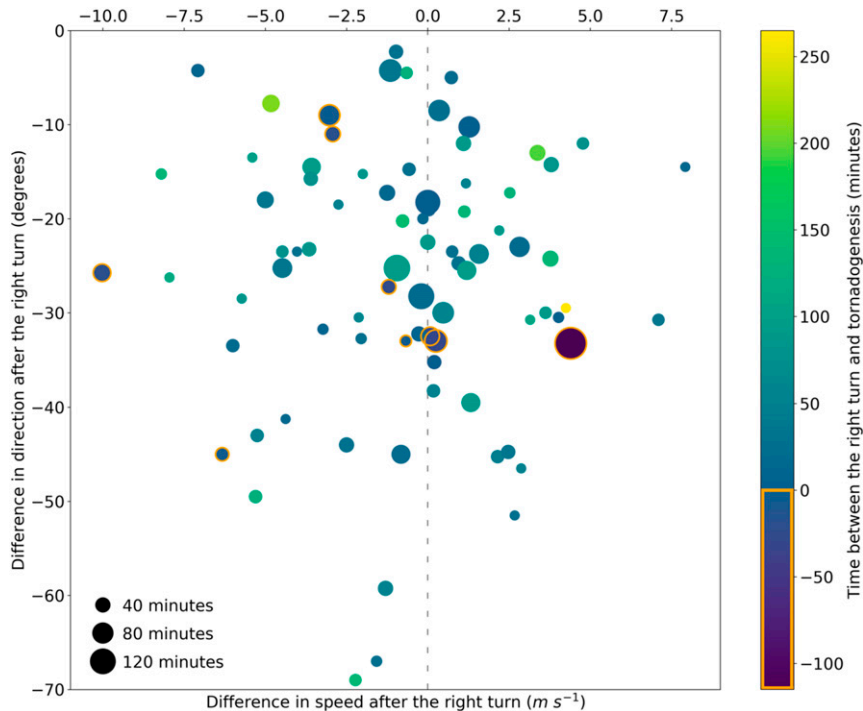
FIG. 2. Scatterplot showing storm and tornado characteristics for the 90 right-turning tornadic supercells. Differences in speed and direction during the right turn are plotted on the *x* and *y* axes, respectively. A negative directional difference indicates a clockwise turn (this is the case for all storms plotted here) and a negative/positive speed difference indicates a slower/faster post-turn storm motion. The size of each marker indicates the time that elapsed between first echo and the right turn, and the color represents the time elapsed between the right turn and tornadogenesis. Storms that produced a tornado before turning right are outlined in orange. Example markers representing different right-turn times (i.e., marker sizes) are shown in the bottom-left corner.

during the first 20 min of the storm's life cycle (initial), the 20-min period 15–35 min prior to the time of the right turn (preturn), and the 20-min period 15–35 min after the time of the right turn (post-turn) are also shown. The 15–35-min periods are chosen so that the resulting mean storm motion before or after the turn is not influenced by storm motions after or before the turn, respectively. If a storm turned right 35 min after initiation, the initial and pre-turn motions are identical. If a storm turned right < 35 min after initiation, the preturn motion is calculated using the instantaneous motions from as many volume times that are available during the $15 - n$-min window prior to the turn, where n is the time of the turn. These motions are rotated such that the initial storm motion for each storm is aligned with the *x* axis (270°). Tornadic storms tend to move faster than nontornadic storms ($>1\,\mathrm{m\,s^{-1}}$) during the initial, preturn, and post-turn phases. Tornadic storms slow slightly more during the right turn than nontornadic storms (roughly 25% more), while nontornadic storms exhibit a slightly larger turn to the right of preturn motion (by about 1.5°); these differences are insignificant, but may be relevant for operational purposes and should be tested further with more data points.

The time of tornadogenesis is probably more strongly influenced by storm-scale details or environmental inhomogeneities than the time of the right turn, but some general characteristics of the time of tornadogenesis were examined.

Of the 90 tornadic supercells that exhibited a right turn, the mean time from initial cell development to tornadogenesis was about 99 min with a standard deviation of about 56 min. The time of tornadogenesis ranged from as low as 15 min after cell development to 285 min. These characteristics do not change substantially if EF0 tornadoes are omitted; of the remaining 56 EF1 or greater tornadoes, the mean time of tornadogenesis after convection initiation is around 109 min with a standard deviation near 55 min. Figure 2 shows a scatterplot of the duration between the time of the right turn and the time of tornadogenesis (for all 90 tornadic supercells) and other storm characteristics, including the change in speed and direction during the right turn as well as the time of the right turn. Do storms that undergo larger changes in direction during the right turn produce tornadoes more quickly after they turn to the right? Based on Fig. 2, it appears not. Do storms that undergo larger changes in speed during the right turn produce tornadoes more quickly after they turn to the right? Based on Fig. 2, it appears not. Although the mean post-turn speed is less than the mean preturn speed for the tornadic supercells (e.g., Table 1), many of the storm speeds increased after the right turn. The difference between preturn and post-turn speeds is not significant (Table 1). Finally, do storms that take longer to turn to the right produce tornadoes more or less quickly after
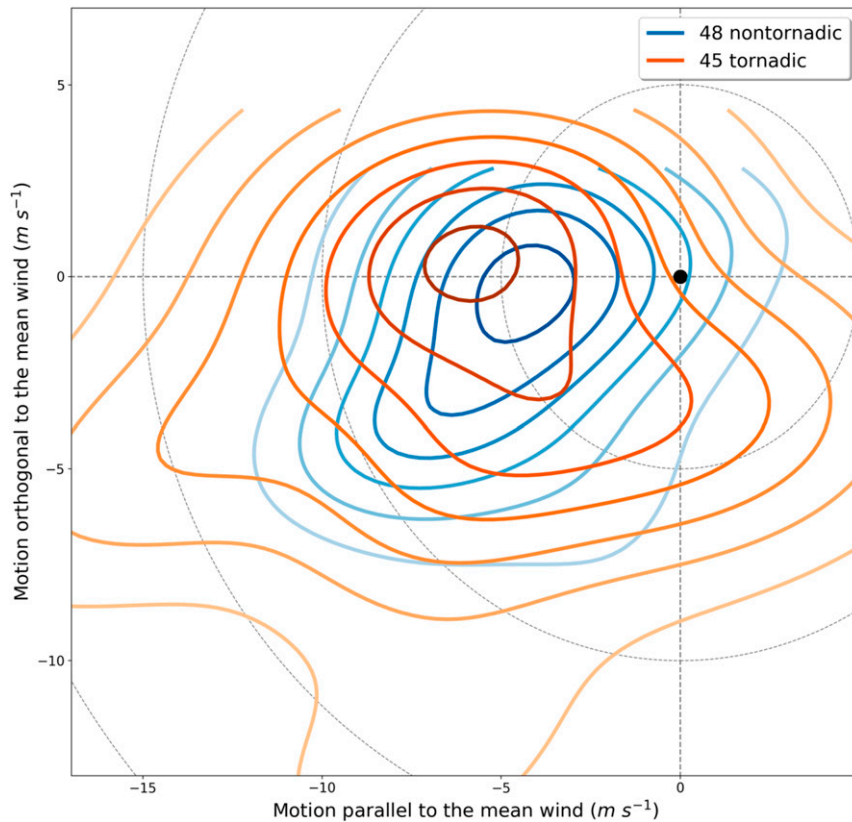
FIG. 3. Kernel density estimation (KDE) of the initial storm motions of 48 nontornadic and 45 tornadic supercells analyzed in a coordinate system with the 0–6-km non-pressure-weighted mean wind at the origin (represented by the black dot). Contours represent constant KDE values, with the maximum density of storm motions for each subset located in each bull's-eye. The tornadic subset is plotted in shades of red and orange and the nontornadic subset is plotted in shades of blue. The mean wind was derived from the first available sounding launched on the storm. Values above and below the x axis represent initial storm motion to the left or right of the mean wind, respectively, and values to the left and right of the y axis represent motions slower or faster than the mean wind.

they turn to the right? Based on Fig. 2, it appears not. Linearly regressing some of these variables against the time of tornadogenesis yielded negatively sloped trend lines, but r^2 values less than 0.01 indicate that they are very unlikely to be useful to forecasters.[6]

Thus, it appears that there are no significant differences in the right-turn characteristics described above between tornadic and nontornadic supercells. These findings are not surprising given observed storm-scale similarities between tornadic and nontornadic supercells (e.g., Markowski et al. 2011). There are also no significant relationships between characteristics of the supercell right turn and subsequent tornadogenesis. Thus far, we

have only analyzed storm and tornado track characteristics and not taken environmental information into account. The influences of different environmental conditions on right-turn characteristics are explored in the next section.

b. Environmental influences on characteristics of the right turn

1) INITIAL CELL MOTION

If the initial cell is advected by the flow and not strongly influenced by cell propagation, its motion should be close to the mean wind in the vertical layer occupied by the cell. The non-pressure-weighted 0–6 km AGL layer is commonly used here and is also used in the original Bunkers storm motion calculation (Bunkers et al. 2000). Figure 3 shows a kernel density estimation (KDE) of the distributions of initial cell motion for tornadic (red/orange) and nontornadic (blue) supercells. KDE is a smoothing method that assigns each data point a shape (or "kernel"), which can then be integrated across the domain to produce smoothed, two-dimensional

---

[6] Of the 90 tornadic supercells that exhibited a clear right turn, 79 of them produced a tornado after the right turn and 11 produced a tornado before the right turn. These 11 storms were not included in the analysis relating the time of the right turn to the duration between the right turn and tornadogenesis.

maps (e.g., Anderson-Frey et al. 2016). Rather than showing scatterplots containing hundreds of points, we show KDEs to more clearly show denser regions and differences between distributions. In Fig. 3, "initial" motion refers to the average cell motion during the first 20 min of its lifespan. Initial cell motion in each case was rotated so that the 0–6 km AGL (non-pressure-weighted) mean wind pointed along the positive x axis. The mean wind was then subtracted from the initial cell motion. After disregarding soundings with insufficient data for the mean-wind calculation and selecting only one sounding for each storm located within inflow, initial cell motions were matched with 93 soundings (45 tornadic and 48 nontornadic). Figure 3 shows that both tornadic and nontornadic supercells move slower than the 0–6-km (non-pressure-weighted) mean wind speed during the first 20 min of their life cycle. There is a signal that tornadic supercells move slower (with respect to the mean wind) than nontornadic supercells, but this difference is not significant. Initial cell motion is generally aligned with but slower than the 0–6-km mean wind, which is consistent with previous findings (e.g., Bluestein and Parker 1993; Weisman and Rotunno 2000).

The fact that initial cell motion is consistently slower than the 0–6-km mean wind suggests that the layer relevant to cell advection is shallower than 6 km. In testing various layers within the 0–6-km layer, mean wind speeds from 0 to 3 km AGL tend to best approximate initial cell speed (not shown). In this layer, cell speed was roughly the same as the mean wind speed but was directed well to the right of it (roughly $5 \, \mathrm{m \, s^{-1}}$ orthogonal to the right of the mean wind on average). Consistent with the early idealized simulations of Rotunno and Klemp (1982), this suggests that cell propagation has an important influence on cell motion very early in the cell's lifetime, a result that is perhaps under-appreciated in supercell motion literature and forecasting applications.

If the propagative effects early in the cell life cycle are dominated by p'_D (e.g., Davies-Jones 2002), including some measure of vertical wind shear should improve the estimate of initial cell motion. To measure this objectively, we used an approach similar to Bunkers et al. (2000) to combine the influence of advection and propagation. Using this method, our estimate of initial cell motion is defined as follows:

$$\mathbf{v}_i = A\mathbf{v}_{\mathrm{mw}} + D\left(\frac{\mathbf{v}_{\mathrm{wd}} \times \hat{\mathbf{k}}}{|\mathbf{v}_{\mathrm{wd}}|}\right), \tag{4}$$

where $\mathbf{v}_i$ is the vector estimate of initial cell motion (m s^{-1}), A is a fraction (from 0 to 1) representing the relative influence of $\mathbf{v}_{\mathrm{mw}}$, $\mathbf{v}_{\mathrm{mw}}$ is the mean wind in a given layer, D represents the magnitude of the deviation of initial motion from the mean wind orthogonal to $\mathbf{v}_{\mathrm{wd}}$ (m s^{-1}), and $\mathbf{v}_{\mathrm{wd}}$ is the vector wind difference in a given layer. As D increases, the influence of shear-orthogonal propagation (represented by $\mathbf{v}_{\mathrm{wd}}$) with respect to advection (represented by $\mathbf{v}_{\mathrm{mw}}$) increases. We tested various layers for the mean wind and wind difference calculations, ranging from 0–2 to 0–6 km AGL for the mean wind and from 0–2 to 3–5 km AGL for the wind difference. This yielded multiple estimates of $\mathbf{v}_i$ that were compared by calculating the

mean absolute error between estimated and observed $\mathbf{v}_i$ for each case.

This analysis reveals that when only accounting for advection (i.e., $D = 0$), estimating $\mathbf{v}_i$ as roughly two-thirds ($A = 0.67$) of the 0–6-km mean wind is more accurate than using any other layer (mean absolute error = 5.1 m s^{-1}). This is consistent with Fig. 3 in that initial cell motion tends to be aligned with and slower than the 0–6-km mean wind, and the fact that advection *and* propagation in lower layers influence initial motion. This estimate is actually more accurate than any combination of advection and propagation! However, increased physical understanding of the relevant advective and propagative processes is gained when examining varying layers of $\mathbf{v}_{\mathrm{mw}}$ and $\mathbf{v}_{\mathrm{wd}}$. In doing so, defining $A = 1.0$ and using 0–4-km $\mathbf{v}_{\mathrm{mw}}$, 0–2-km $\mathbf{v}_{\mathrm{wd}}$, and $D = 4.0 \, \mathrm{m \, s^{-1}}$ yields the lowest mean absolute error (5.7 m s^{-1}). The distribution of initial cell motions around this estimate is shown in Fig. 4 (blue) as well as the estimate bias (orange, $u = -1.2 \, \mathrm{m \, s^{-1}}$ and $v = 1.0 \, \mathrm{m \, s^{-1}}$). This is consistent with our conceptual understanding of supercell evolution: advection is driven by the development of the midlevel updraft, and off-shear propagation (due to both p'_L and p'_{NL} in environments with vertically veering wind shear) is driven by the updraft and developing mesocyclone, which is strongest beneath the level of maximum vertical velocity due to tilting and stretching. The result is a cell motion influenced by low-/midlevel advection and low-level propagation with the first 20 min after convection initiation.

2) POST-TURN CELL MOTION

Bunkers storm motion (Bunkers et al. 2000) is commonly used to predict the motion of right- and left-moving supercells in supportive environments using only the environmental wind profile. Figure 5, similar to Fig. 3 except normalized around Bunkers-right storm motion, shows that Bunkers-right storm motion provides a good estimate of the post-turn storm motion for the supercells in this dataset ($n = 72$ in this analysis due to many soundings containing insufficient data to calculate Bunkers storm motion). This is true for both tornadic and nontornadic supercells. However, Fig. 5 shows that post-turn motion for nontornadic storms tends to lie to the left of Bunkers-right storm motion while post-turn motion for tornadic storms tends to lie to the right. On average, the mean deviance of the post-turn motion orthogonal to Bunkers-right motion for tornadic storms is 2.2 m s^{-1} while the same for nontornadic storms is 0.8 m s^{-1}. While this difference is not quite significant at the 90% confidence level, it is applicable to real-time forecasting and a larger sample size may yield a significant result. Of the 72 storms analyzed in Fig. 5, 45 exhibit post-turn motion to the right of Bunkers-right and 26 to the left. Of the 45 that deviate rightward, 58% are tornadic. More importantly, of the 26 that deviate leftward, 35% are tornadic. In summary, a storm that exhibits post-turn motion left of the Bunkers-right estimate is less likely to be tornadic. This is consistent with Bunkers (2018), who found that tornadic supercells deviated farther rightward than nontornadic ones. This result is strengthened by CP20 who focused on the time near and shortly after tornado occurrence. Because the mean time between the right turn and tornadogenesis in this dataset is almost one hour, this suggests that comparing the
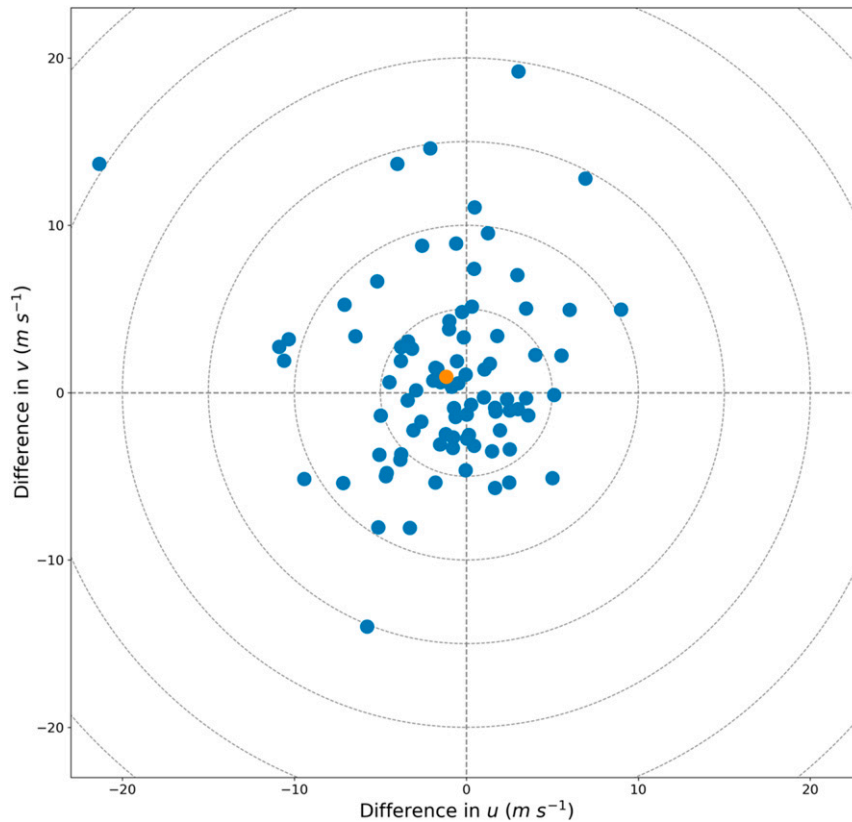
FIG. 4. Scatterplot of initial storm motion estimates calculated using Eq. (4) (blue) and the mean bias (orange). In Eq. (4), $\mathbf{v}_{mw}$ is calculated in the 0–4-km layer, $\mathbf{v}_{wd}$ is calculated in the 0–2-km layer, and $D = 4.0 \, \mathrm{m \, s^{-1}}$. The mean bias is $u = -1.2 \, \mathrm{m \, s^{-1}}$ and $v = 1.0 \, \mathrm{m \, s^{-1}}$.

post-turn motion with expected Bunkers-right motion may yield increased predictive skill of tornado potential (e.g., Bunkers 2018).

3) TIME OF THE RIGHT TURN

In an effort to better predict the time of the right turn in certain environments, different environmental parameters are plotted against the time of the right turn. Surface-based CAPE (SBCAPE) and CIN (SBCIN) are shown first (see Figs. 6a,b). After restricting the soundings based on data availability and location with respect to the inflow sector, 75 soundings were paired with 35 tornadic and 40 nontornadic storms. Environmental SBCAPE near the tornadic and nontornadic supercells ranges from close to 0 to >5000 J kg^{-1} while SBCIN ranges from 0 to around -350 J kg^{-1}. These distributions are similar between the tornadic (orange) and nontornadic (blue) subsets, although not surprisingly mean SBCIN is significantly less (at the 95% confidence level) in the tornadic environments (-44 J kg^{-1}) than in the nontornadic ones (-81 J kg^{-1}). No clear relationships exist between the amount of SBCAPE or SBCIN and the time of the right turn for either tornadic or nontornadic supercells.

Mixed-layer CAPE (MLCAPE) and CIN (MLCIN), calculated using mixed conditions in the lowest 100 hPa, were evaluated in the same way (Fig. 6c,d). The ranges are similar to those of SBCAPE and SBCIN. Based on Figs. 6c and 6d, no clear relationships exist between the amount of MLCAPE or

MLCIN and the time of the right turn for either tornadic or nontornadic supercells. Similar to SBCIN, mean MLCIN was significantly less (at the 90% confidence level) in tornadic environments (-53 J kg^{-1}) than in nontornadic ones (-82 J kg^{-1}).

Thinking the time of the right turn may be more strongly influenced by low-level buoyancy, we examined 0–3 km AGL CAPE. The surface parcel was used for this calculation, and findings are shown in Fig. 7. No clear relationships exist between the amount of 0–3-km CAPE and the time of the right turn. However, mean 0–3-km CAPE is significantly larger (at the 99% confidence level) in tornadic environments (63 J kg^{-1}) than in nontornadic ones (37 J kg^{-1}). CP20 also found larger 0–3-km CAPE for tornadic soundings than nontornadic ones, but not significantly so. This is because this study defines a sounding as tornadic if the storm produced a tornado at any point and focuses on soundings launched earliest in the storm's life cycle. As such, some of the 0–3-km CAPE values incorporated into this analysis may not be representative of the storm inflow near the time of tornadogenesis (or at failed tornadogenesis or other times for nontornadic supercells).

We also examined the possible influence of boundary layer humidity on the time of the right turn, analyzed here in terms of the mixed-layer lifted condensation level (MLLCL). No significant trends exist (Fig. 8), whether outliers are excluded or not (e.g., the soundings with MLLCLs near 2500 m).
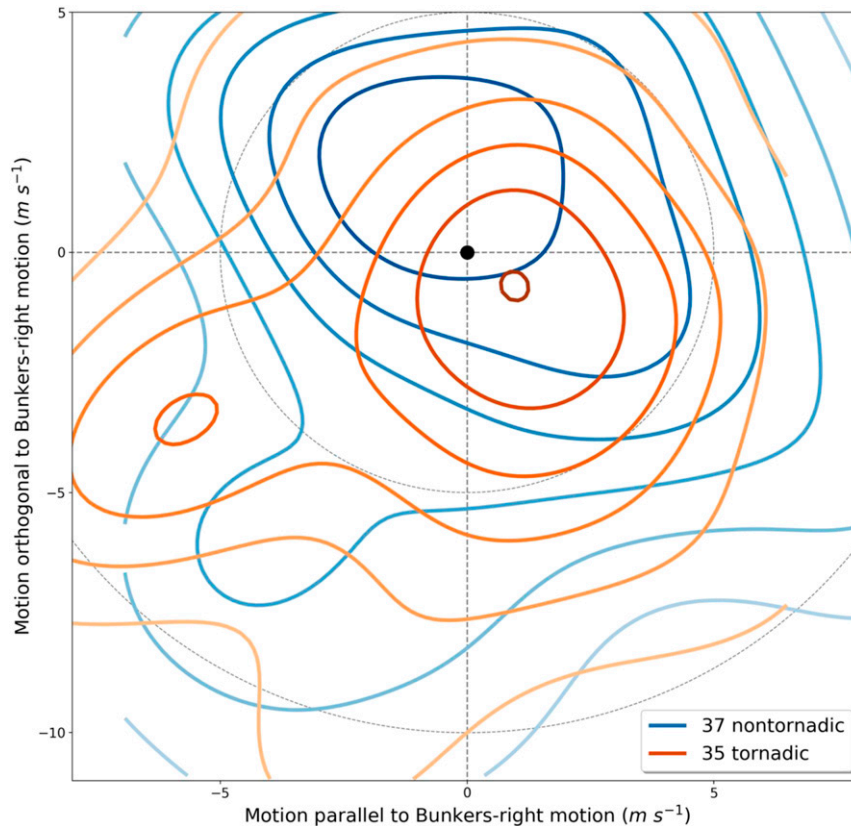
FIG. 5. As in Fig. 3, but for post-turn storm motions compared to Bunkers-right storm motion
for 37 nontornadic and 35 tornadic storms.

Unsurprisingly, the means of the MLLCLs in the tornadic (1166 m) and nontornadic (1333 m) subsets are statistically different at the 90% confidence level.

Storm motion is also influenced by internal, microphysical processes like how quickly the cold pool spreads, cold pool depth, etc. To some degree, these processes are related to environmental parameters like downdraft CAPE (DCAPE). However, no significant relationship exists between DCAPE (calculated using the parcel with the lowest equivalent potential temperature in the lowest 400 hPa AGL) and the time of the right turn (Fig. 9). The means and distributions of DCAPE are very similar between the tornadic and nontornadic subsets.

From a kinematic standpoint, the right turn (or split) of the main updraft occurs as the result of both p'_{NL} enhancing the right and left flanks and p'_L enhancing the right flank as hodograph curvature increases. The relative magnitudes of these processes may be related to the relative magnitudes of crosswise and streamwise vorticity in the environment, respectively (e.g., Weisman and Rotunno 2000). Increasingly crosswise vorticity favors minimal initial collocation between vertical velocity and vertical vorticity maxima, promoting storm splitting through p'_{NL}, whereas increasingly streamwise vorticity favors larger collocation and rightward deviance through an increasing contribution from p'_L. Because of the contributions to rightward deviance from tilting of streamwise vorticity, we hypothesize that the timing of the right turn is inversely related

to the amount of initially streamwise, low-level horizontal vorticity in the environment, often measured in terms of SRH. In addition to streamwise vorticity magnitude, SRH is also a function of storm-relative wind speed; the separate influences of streamwise vorticity magnitude and storm-relative wind speed may influence supercell characteristics differently (Peters et al. 2020). We analyze each component separately here. We also test the hypothesis that the timing of the right turn is inversely related to the amount of initially crosswise, low-level horizontal vorticity, which represents a right turn resulting from storm splitting.

Figure 10 shows scatterplots of the time of the right turn in the tornadic and nontornadic supercell subsets with respect to the mean storm-relative wind magnitudes in various layers of the environment. The mean storm-relative wind vector in each layer was found by calculating the layer-mean ground-relative wind vector and subtracting the observed, initial storm motion vector (i.e., the average storm motion vector during the first 20 min of the storm's life-span). In the three layers analyzed—0–0.5, 0–1, and 0–3 km AGL—there are no statistically significant relationships between the mean storm-relative wind magnitude and the time of the right turn. Mean storm-relative wind magnitudes decrease with height from a mean near $14 \, m \, s^{-1}$ in the 0–0.5 km AGL layer to roughly $7.5 \, m \, s^{-1}$ in the 0–3 km AGL layer. In the 20 min after the initial right turn, tornadic environmentstend to have slightly faster mean storm-relative winds than
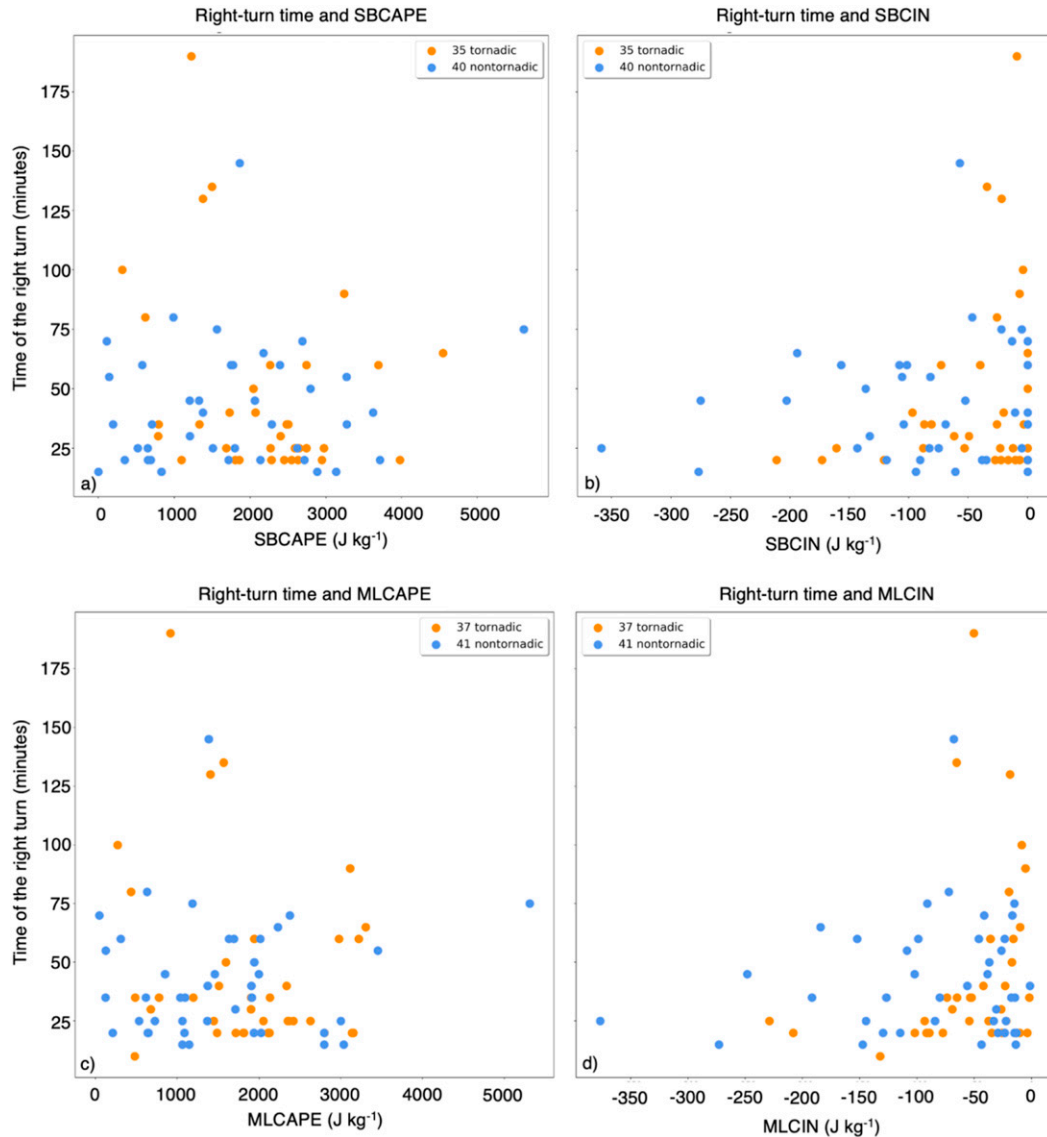
FIG. 6. Scatterplots showing the time of the right turn against (a) SBCAPE, (b) SBCIN, (c) MLCAPE, and (d) MLCIN for the tornadic and nontornadic subsets. Tornadic points are orange and nontornadic ones are blue.

nontornadic ones by about $1\,\mathrm{m\,s^{-1}}$, but this difference is insignificant.[7]

Mean streamwise vorticity magnitudes are analyzed next and exhibit a similar lack of relationship to the time of the right turn (Fig. 11). The mean horizontal vorticity magnitude was found in each layer by averaging the horizontal vorticity vector components from the vertical wind profile (assuming no horizontal

gradients in vertical velocity) at each sounding level within the layer. Then, mean streamwise horizontal vorticity was found by projecting the mean horizontal vorticity vector onto the mean storm-relative wind vector. There is no significant relationship between the time of the right turn and mean streamwise vorticity magnitude in any of the layers examined (shown for 0–0.5, 0–1, and 0–3 km AGL in Fig. 11). An interesting result is that, while no significant trend exists, environments containing 0–1 km AGL mean streamwise vorticity of at least $0.012\,\mathrm{s^{-1}}$ are associated with supercellular right turns roughly 60 min or less into the storm's life cycle. (In the analyses using the right-turn times found by the second and third authors, one or two storms exceed this threshold, but the same qualitative result is consistent). Mean 0–1 km AGL streamwise vorticity values less than this are associated with a wider range of right-turn times.

---

[7] Note that CP20 find substantially larger storm-relative wind speeds for tornadic soundings compared to nontornadic soundings from a similar dataset; the difference here is that the present study focuses on the early evolution of the supercells, whereas that study narrowed the focus to soundings taken near the time of the tornado.
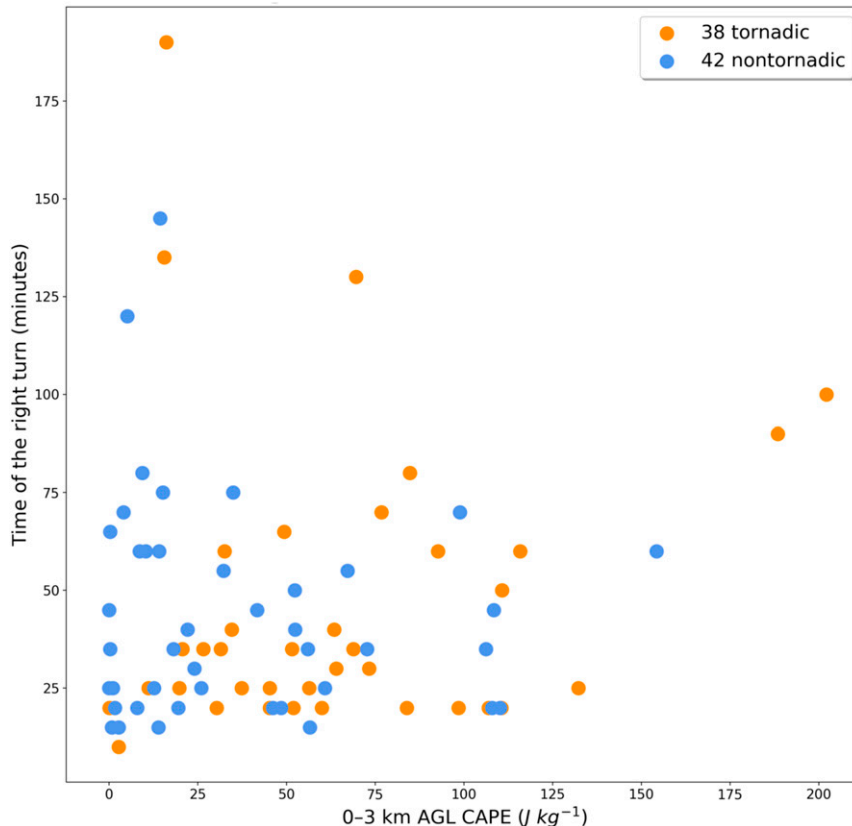
FIG. 7. As in Fig. 6, but for 0–3-km SBCAPE.

Mean streamwise vorticity magnitudes increase in both tornadic and nontornadic environments as the analyzed layer gets thinner and closer to the surface. In fact, horizontal vorticity magnitudes are roughly three times larger in the 0–0.5 km AGL layer than in the 0–3 km AGL layer (0.015 and 0.005 s^{-1}; note the differences in the x-axis limits). Somewhat surprisingly, differences between mean streamwise vorticity magnitudes in the tornadic and nontornadic environments are insignificant. Streamwise vorticity magnitudes in tornadic environments are slightly larger in the 0–1- and 0–3-km layers but are actually slightly smaller in the 0–0.5-km layer than those in nontornadic environments. SRH calculated in the same layers follows suit; mean 0–1 and 0–3-km SRH are larger in tornadic environments but 0–0.5-km SRH is very similar in the tornadic and nontornadic subsets (not shown). Recall that CP20 included a time-threshold on defining a sounding as "tornadic" (the tornado occurred within 6 min before to 90 min after the sounding launch), whereas we do not apply such a threshold in this study. The conclusion here is that, near the time of the right turn, supercells destined to be tornadic do not encounter significantly larger or smaller streamwise vorticity and SRH than supercells destined to be nontornadic. This adds some complexity to the growing body of literature examining the nature of near-surface horizontal vorticity and its possible influence on tornado potential (e.g., Esterheld and Giuliano 2008; Coffer and Parker 2017).

Is the amount of crosswise vorticity present in the environment related to the time of the right turn? Based on Fig. 12, it appears not. Mean crosswise vorticity in each layer was found as the vector difference between the mean horizontal vorticity and mean streamwise vorticity vectors. Similar to mean streamwise vorticity, mean crosswise vorticity increases as the analyzed layer gets thinner and closer to the surface. Interestingly, mean crosswise vorticity magnitudes are not significantly different between the tornadic and nontornadic subsets in any of these layers.

4. Discussion

Of the 220 supercell tracks in this database, the authors found between 169 and 211 that turned right. Why did not all of the supercells turn right? As recognized in Rasmussen and Blanchard (1998) and Bunkers et al. (2000), and others, a number of factors influence storm motion, perhaps the most prevalent being the presence of environmental heterogeneities like storm-generated boundaries, fronts, horizontal convective rolls, etc. Boundaries like these are often accompanied by a local maximum in surface vertical vorticity, upward motion, and wind shear, all of which may enhance the environment in terms of supercell potential and alter the storm motion. Spatial or temporal environmental changes may also occur along the storm tracks in the absence of any well-defined boundaries, for
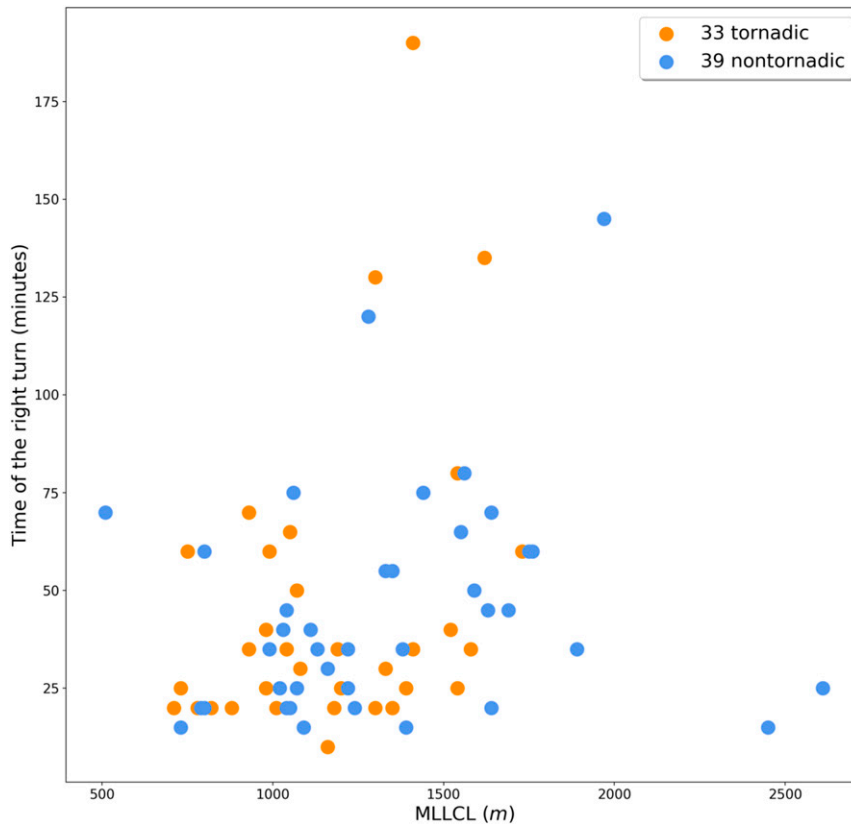
FIG. 8. As in Fig. 6, but for MLLCL.

example, as the storm gradually moves into a region containing more or less vertical wind shear or CAPE (e.g., Richardson et al. 2007), or as the boundary layer gradually cools and decouples near sunset (e.g., Coffer and Parker 2015). Furthermore, intra-storm characteristics like cold pool properties, updraft pulses, precipitation distribution, etc., or influences from nearby storms all affect supercell motion in a complex manner. In the remaining storms, we hypothesize that some of these factors influenced storm motion enough to offset the expected impacts of linear and nonlinear pressure perturbations. Of the storms that turned right, some exhibited gradual turns while others turned very abruptly. Whether the abruptness is driven by rapid changes in storm-internal processes or environmental inhomogeneities, or a combination of both, is unknown.

It is possible for environments to favor a right-moving supercell that moves "to the left" of the mean wind. In the United States, environments supporting this evolution may be characterized by a veering wind profile with 0–6-km shear oriented tangent to isotachs in hodograph space (e.g., Zeitler and Bunkers 2005; Bunkers and Doswell 2016; Bluestein et al. 2019). This can yield expected pre- and post-turn motions along or across a radial, indicating a change only in speed or a directional change to the left. Based on the methods we used, cases in which this may have occurred were neglected.

Of the environmental parameters examined here in the vicinity of 169 right-turning tornadic and nontornadic supercells, none exhibited a strong correlation to the time of the right turn.

Why? One possible explanation is that although the soundings analyzed here were launched within the inflow sector, there was still large spread in their storm-relative locations (with respect to distance and angle from storm motion). Storm-environment modifications may have resulted in somewhat heterogeneous environments across the inflow region (e.g., Wade et al. 2018; CP20), which would hinder the identification of the relationships we seek. To help address this, we performed linear regressions between the time of the right turn and the aforementioned environmental parameters at various distances and angles from the storm across the inflow sector, but these did not reveal any significant variations in trends in any particular region (not shown). Perhaps more importantly though, this analysis included soundings launched during any phase of the supercell's life cycle. Restraining the sounding analysis by distance and angle from the storm as well as time into the storm's life cycle yielded insufficient data to examine any relationships. For example, restricting the soundings to those launched within 30 min of the time of the right turn for each case resulted in roughly half of the number of cases shown in Figs. 6–12. In summary, readers should not conclude from this study that characteristics of the right turn in supercells are not related to environmental conditions. Analysis of soundings in the inflow region targeting specific phases of the supercell life cycle, specifically the developmental phase, may reveal stronger relationships between environmental parameters and the storm characteristics examined here.
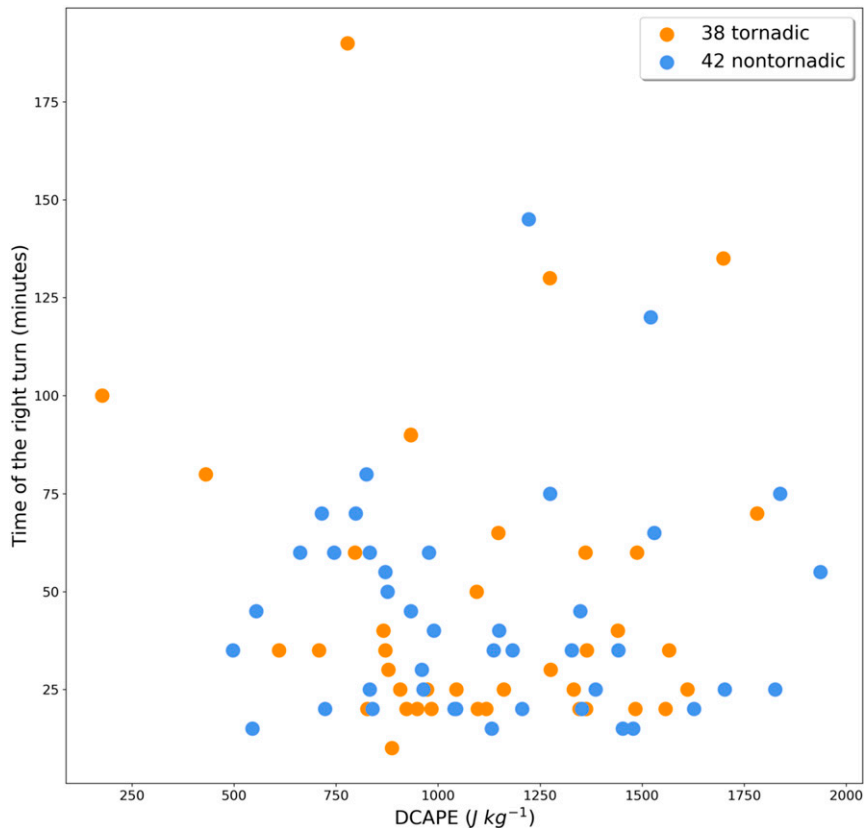
FIG. 9. As in Fig. 6, but for DCAPE.

Specifically, we did not find a significant relationship between the time of the right turn and the amount of streamwise vorticity (or SRH) in various layers of the environment. However, we did find a general threshold of 0–1 km AGL streamwise vorticity separating groups of storms that either took much more or much less time to turn right (see Fig. 11). Environments containing less than around $0.012 \, \mathrm{s}^{-1}$ mean 0–1-km streamwise horizontal vorticity supported a larger

range of supercell right-turn times than those containing more streamwise vorticity. Every storm in an environment characterized by $\geq 0.012 \, \mathrm{s}^{-1}$ mean 0–1 km AGL streamwise horizontal vorticity turned right within 60 min. Similar analysis of environmental 0–1-km SRH (calculated separately using the initial and post-turn storm motions) revealed a very similar threshold around $300 \, \mathrm{m}^2 \, \mathrm{s}^{-2}$. These findings suggest that 0–1-km SRH does influence the time of
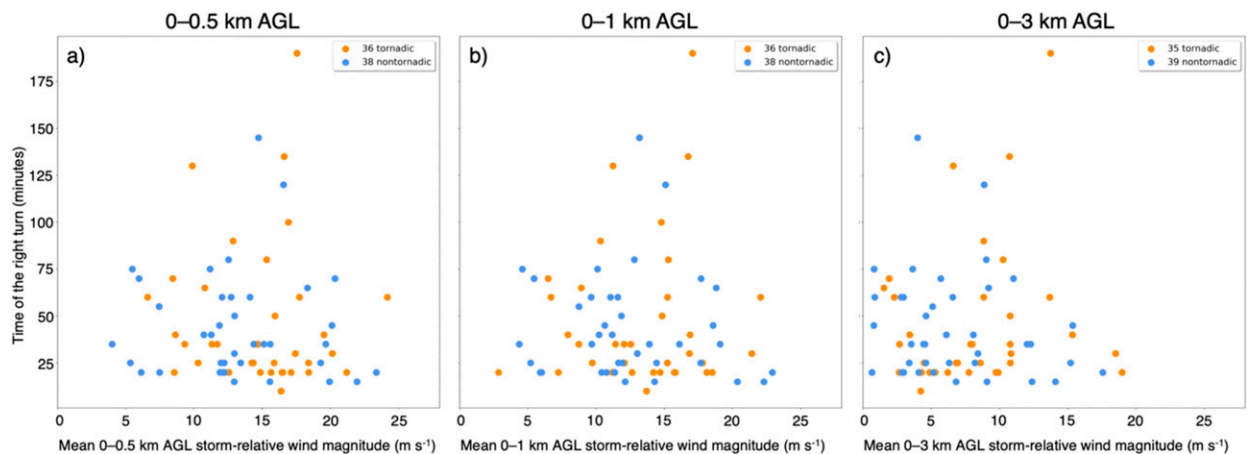
FIG. 10. As in Fig. 6, but for (a) 0–0.5, (b) 0–1 AGL, and (c) 0–3 km AGL mean storm-relative wind speed.
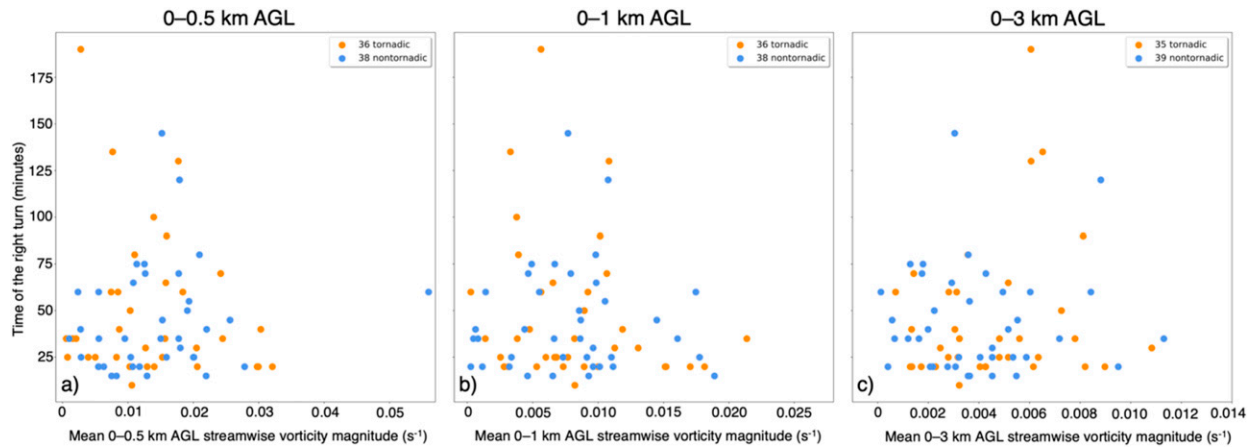
FIG. 11. As in Fig. 10, but for mean streamwise horizontal vorticity magnitude in each layer. The scale of the *x* axis in (b) is roughly half of the scale in (a), and the scale of the *x* axis in (c) is half of the scale in (b).

the right turn but the strength of that influence is small in environments with lesser SRH (e.g., $<300\,\mathrm{m}^2\,\mathrm{s}^{-2}$). In these more common environments, other factors like environmental inhomogeneities and storm-scale details are more important in governing the time of the right turn than in extreme environments. While this finding should not be interpreted as a hard threshold, it is relevant for forecasters predicting supercell development and path in real-time operations.

We also found a lack of a significant difference between low-level streamwise and crosswise horizontal vorticity in the environments of tornadic and nontornadic supercells. This is interesting given that larger SRH, especially closer to the surface (e.g., Coffer et al. 2019), is associated with stronger low-level updrafts in turn supporting increased tornado potential. Some studies like Coffer and Parker (2017) specifically explore the detrimental effects of larger low-level crosswise vorticity on robust low-level mesocyclones. However, other recent studies like Guarriello et al. (2018) found that larger near-surface crosswise vorticity favored alignment between the surface vortex and the overlying mesocyclone and vortex

strengthening. Some differences between these studies and ours might be related to the fact that we used high-resolution observed soundings whereas others used model-derived ones. Furthermore, the soundings used in this study were obtained during field projects where target storms were carefully chosen because they were in favorable environments. It is possible that low-level streamwise vorticity might emerge as a more significant discriminator between tornadic and nontornadic environments if more marginal environments are included. Finally, we considered a sounding "tornadic" if the target storm produced a tornado at any point in its life cycle. While our methods—focusing on the early portion of each storm's life cycle—prevented it, analyses incorporating a time threshold when distinguishing "tornadic" and "nontornadic" cases (e.g., CP20) might yield larger differences. Future work should continue to explore the physical processes relating environmental vorticity orientation to low-level mesocyclone characteristics.

On average, the observed storm motion during the first 20 min of the storm's life cycle was in approximately the same direction as, but slower than, the 0–6-km mean wind. The mean
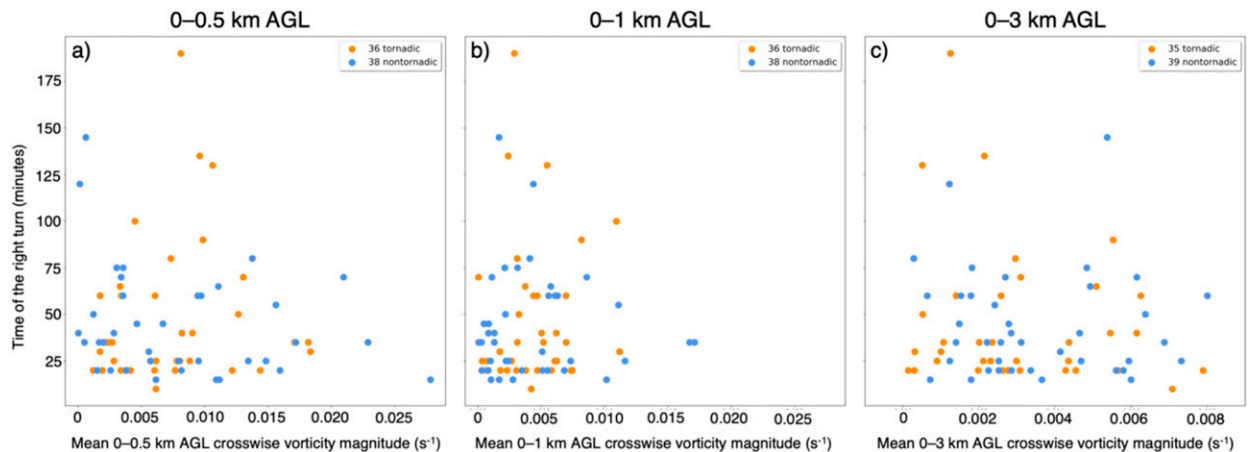

FIG. 12. As in Fig. 10, but for mean crosswise horizontal vorticity magnitude in each layer. The scale of the *x* axes in (a) and (b) is the same, and the scale of the *x* axis in (c) is roughly one-third of those in (a) and (b).
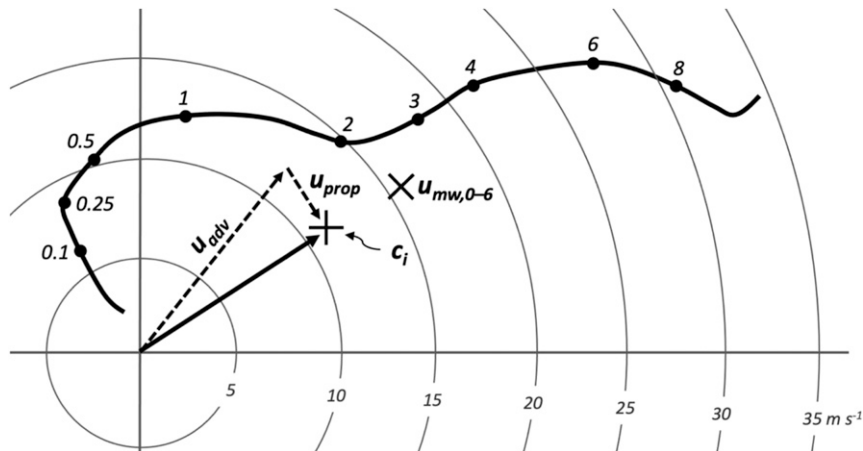
FIG. 13. Schematic summarizing the effects of 0–4-km advection (u_{adv}) and 0–2-km propagation (u_{prop}) on initial cell motion (c_i), which falls in the same direction as the 0–6-km mean wind ($u_{mw,0-6}$) at roughly two-thirds the speed. This ground-relative wind profile is derived from the storm-relative tornadic profile in Fig. 7 of CP20. Rings are shown every 5 m s^{-1}, and heights (km) are plotted.

wind in lower layers served as a better estimate of initial cell speed but pointed to the left of initial cell bearing. In fact, the mean wind in any layer examined did not remove these biases in both speed and direction simultaneously; the mean wind was either too slow or misdirected relative to storm motion. The cause is that p'_D has a noticeable influence on cell motion even during the early developmental phase. This is due to a combination of p'_L and p'_{NL} that induces propagation downshear (p'_L) and to the right of the mean shear vector (p'_L and p'_{NL}) in environments with vertically veering vertical wind shear. A characteristic wind profile in the vicinity of tornadic storms (adapted from Fig. 7 in CP20) is shown in Fig. 13 to summarize these effects. The advective component is aligned with the 0–4-km mean wind and the off-shear propagative component is orthogonal to the 0–2-km shear vector, resulting in an initial cell motion oriented in the same direction as the 0–6-km mean wind at roughly two-thirds the speed. In summary, these findings reiterate that the 0–6-km mean wind is not an optimal estimate of initial cell motion. The 0–6-km mean wind tends to be a good estimate of initial cell bearing, but initial cell speed is more strongly related to the wind profile in lower layers because propagation effects impact motion early in the cell life cycle.

5. Summary

This study analyzed 902 soundings and 220 storm tracks that were observed during field campaigns from 1994 to 2019. These soundings contain greater vertical resolution than the typical radiosonde launches in national, operational sounding networks, especially in the lowest 1–2 km AGL. This dataset is used to examine relationships between environmental conditions and supercell characteristics, particularly related to the right turn. This study mainly focused on addressing the following questions:

- How long does it take a developing supercell to turn right? How is this time scale influenced by environmental characteristics?

- Is the initial cell motion (prior to the right turn) generally aligned with the mean wind or shear in different layers?
- Are the answers to the above questions different for supercells destined to be tornadic or nontornadic?

General storm characteristics between tornadic and nontornadic storms were not significantly different. In particular, the time between cell appearance on radar and the right turn was roughly 44 min with a standard deviation of 25–30 min. On average, storms tended to slow slightly (around 0.2 m s^{-1}) and deviate 17°–20° (with respect to initial motion) during the right turn. These results are readily applicable for operational forecasters, field coordinators, and others in predicting the time of the right turn, resulting storm motion, and development of supercellular hazards.

We did not find significant relationships between any environmental parameters examined here and the time of the supercell right turn. As discussed above, this does not mean that these relationships do not exist. It is possible that these relationships exist on scales that we are unable to resolve in this study, especially temporal ones. This may also be due to the subjective techniques that the coauthors used to identify the time of the right turn. Soundings close to the storm and prior to the right turn should be examined, but placing those restraints on this dataset yields a sample size too small to detect any meaningful trends. Future field campaigns that collect observations early in storms' life cycles would help shed light on these relationships.

Initial cell bearing and speed were not well represented by the mean wind in any one layer. The best estimate of initial cell motion was in the direction of the 0–6-km mean wind at roughly two-thirds the speed. This is evidence that, in addition to advection, propagation in lower layers influences cell motion within 20 min after convection initiation. We showed that a combination of 0–4-km advection (related to the developing updraft) and 0–2-km off-shear propagation (related to the

developing mesocyclone) most strongly influenced initial cell motion. These findings show that the effects of p' are important for *developing* supercells and should not be ignored when approximating their future paths.

In our analysis and final schematic, we simplified the propagative component to one term oriented orthogonal to the shear vector. This limits the representation of downshear propagation induced by p'_L, which would influence the deviance of initial cell motion from the 0–4-km mean wind. A future study may decompose supercell motion (during the developmental and mature phases) into advective, downshear propagative, and off-shear propagative components to further assess their relative influences.

Although not the main focus of this study, we identified interesting differences (or lack thereof) between the environments of tornadic and nontornadic supercells. In particular, the tornadic environments in this dataset contained significantly less CIN, more 0–3-km CAPE, and lower LCLs than the nontornadic environments, all of which corroborate many past studies on the topic. On the other hand, there were no significant differences between the tornadic and nontornadic environments in terms of storm-relative wind speeds or the amount of streamwise or crosswise horizontal vorticity. This is unlike some previous studies that found differences in these characteristics between tornadic and nontornadic environments. Some of these differences are probably attributable to the fact that this study focuses on the early part of the supercell's life cycle whereas others are more diverse in when the storm was sampled. Finally, although the difference was not significant, tornadic supercells tended to deviate more to the right of Bunkers-right storm motion after the right turn than nontornadic ones. Of the storms that deviated leftward of Bunkers-right storm motion after the turn, only 35% were tornadic. This is consistent with the positive relationships between increasingly rightward motion and storm-relative wind speeds, SRH, etc., and is relevant for predicting real-time supercellular tornado potential around one hour in advance.

These findings motivate further examination of environmental conditions and supercell characteristics during their developmental phase. In particular, an ongoing project will address the degree to which the background supercell environment is homogeneous. We also hope to examine how storm-internal evolution and/or environmental inhomogeneities influence cell motion. Observations from field campaigns targeting the inflow of developing supercells will be important here. Idealized modeling would be a useful tool to explore these relationships by controlling storm initialization and various environmental conditions of interest. Hopefully, future studies like these will continue to yield insight into how environmental conditions influence supercell development and how these relationships may be useful for real-time prediction hours into the future once a cell develops.

Data availability statement. The data used in this study are stored locally and are available from the authors upon request. Example codes used to generate plots for this study are available online in a GitHub repository at "mdflournoy/supercell-sounding-climo."

REFERENCES

Anderson-Frey, A. K., Y. P. Richardson, A. R. Dean, R. L. Thompson, and B. T. Smith, 2016: Investigation of near-storm environments for tornado events and warnings. *Wea. Forecasting*, **31**, 1771–1790, https://doi.org/10.1175/WAF-D-16-0046.1.

Bluestein, H. B., and S. S. Parker, 1993: Modes of isolated, severe convective storm formation along the dryline. *Mon. Wea. Rev.*, **121**, 1354–1372, https://doi.org/10.1175/1520-0493(1993)121<1354:MOISCS>2.0.CO;2.

——, D. T. Lindsey, D. Bikos, D. W. Reif, and Z. B. Wienhoff, 2019: The relationship between overshooting tops in a tornadic supercell and its radar-observed evolution. *Mon. Wea. Rev.*, **147**, 4151–4176, https://doi.org/10.1175/MWR-D-19-0159.1.

Browning, K. A., 1964: Airflow and precipitation trajectories within severe local storms which travel to the right of the winds. *J. Atmos. Sci.*, **21**, 634–639, https://doi.org/10.1175/1520-0469(1964)021<0634:AAPTWS>2.0.CO;2.

Bunkers, M. J., 2018: Observations of right-moving supercell motion forecast errors. *Wea. Forecasting*, **33**, 145–159, https://doi.org/10.1175/WAF-D-17-0133.1.

——, and C. A. Doswell, 2016: Comments on "Double impact: When both tornadoes and flash floods threaten the same place at the same time." *Wea. Forecasting*, **31**, 1715–1721, https://doi.org/10.1175/WAF-D-16-0116.1.

——, B. A. Klimowski, J. W. Zeitler, R. L. Thompson, and M. L. Weisman, 2000: Predicting supercell motion using a new hodograph technique. *Wea. Forecasting*, **15**, 61–79, https://doi.org/10.1175/1520-0434(2000)015<0061:PSMUAN>2.0.CO;2.

Cai, H., and R. M. Wakimoto, 2001: Retrieved pressure field and its influence on the propagation of a supercell thunderstorm. *Mon. Wea. Rev.*, **129**, 2695–2713, https://doi.org/10.1175/1520-0493(2001)129<2695:RPFAII>2.0.CO;2.

Coffer, B. E., and M. D. Parker, 2015: Impacts of increasing low-level shear on supercells during the early evening transition. *Mon. Wea. Rev.*, **143**, 1945–1969, https://doi.org/10.1175/MWR-D-14-00328.1.

——, and ——, 2017: Simulated supercells in nontornadic and tornadic VORTEX2 environments. *Mon. Wea. Rev.*, **145**, 149–180, https://doi.org/10.1175/MWR-D-16-0226.1.

——, ——, R. L. Thompson, B. T. Smith, and R. E. Jewell, 2019: Using near-ground storm relative helicity in supercell tornado forecasting. *Wea. Forecasting*, **34**, 1417–1435, https://doi.org/10.1175/WAF-D-19-0115.1.

Coniglio, M. C., and M. D. Parker, 2020: Insights into supercells and their environments from three decades of targeted radiosonde observations. *Mon. Wea. Rev.*, **148**, 4893–4915, https://doi.org/10.1175/MWR-D-20-0105.1.

Craven, J. P., and H. E. Brooks, 2004: Baseline climatology of sounding derived parameters associated with deep, moist convection. *Natl. Wea. Dig.*, **28**, 13–24.

Davenport, C. E., and M. D. Parker, 2015: Impact of environmental heterogeneity on the dynamics of a dissipating supercell thunderstorm. *Mon. Wea. Rev.*, **143**, 4244–4277, https://doi.org/10.1175/MWR-D-15-0072.1.

——, C. L. Ziegler, and M. I. Biggerstaff, 2019: Creating a more realistic idealized supercell thunderstorm evolution via incorporation of base-state environmental variability. *Mon. Wea. Rev.*, **147**, 4177–4198, https://doi.org/10.1175/MWR-D-18-0447.1.

Davies, J. M., and R. H. Johns, 1993: Some wind and instability parameters associated with strong and violent tornadoes: 1. Wind shear and helicity. *The Tornado: Its Structure, Dynamics, Prediction, and Hazards*, C. Church et al., Eds., Amer. Geophys. Union, 573–582.

Davies-Jones, R., 1984: Streamwise vorticity: The origin of updraft rotation in supercell storms. *J. Atmos. Sci.*, **41**, 2991–3006, https://doi.org/10.1175/1520-0469(1984)041<2991:SVTOOU>2.0.CO;2.

——, 2002: Linear and nonlinear propagation of supercell storms. *J. Atmos. Sci.*, **59**, 3178–3205, https://doi.org/10.1175/1520-0469(2003)059<3178:LANPOS>2.0.CO;2.

Droegemeier, K. K., S. M. Lazarus, and R. Davies-Jones, 1993: The influence of helicity on numerically simulated convective storms. *Mon. Wea. Rev.*, **121**, 2005–2029, https://doi.org/10.1175/1520-0493(1993)121<2005:TIOHON>2.0.CO;2.

Esterheld, J. M., and D. J. Giuliano, 2008: Discriminating between tornadic and non-tornadic supercells: A new hodograph technique. *Electron. J. Severe Storms Meteor.*, **3** (2), https://ejssm.org/ojs/index.php/ejssm/article/viewArticle/33.

Glickman, T. E., Ed., 2000: *Glossary of Meteorology.* 2nd ed. Amer. Meteor. Soc., 855 pp., http://glossary.ametsoc.org/.

Gropp, M. E., and C. E. Davenport, 2018: The impact of the nocturnal transition on the lifetime and evolution of supercell thunderstorms in the Great Plains. *Wea. Forecasting*, **33**, 1045–1061, https://doi.org/10.1175/WAF-D-17-0150.1.

Guarriello, F., C. J. Nowotarski, and C. C. Epifanio, 2018: Effects of the low-level wind profile on outflow position and near-surface vertical vorticity in simulated supercell thunderstorms. *J. Atmos. Sci.*, **75**, 731–753, https://doi.org/10.1175/JAS-D-17-0174.1.

Klees, A. M., Y. P. Richardson, P. M. Markowski, C. Weiss, J. M. Wurman, and K. K. Kosiba, 2016: Comparison of the tornadic and nontornadic supercells intercepted by VORTEX2 on 10 June 2010. *Mon. Wea. Rev.*, **144**, 3201–3231, https://doi.org/10.1175/MWR-D-15-0345.1.

Lawson, J. R., J. S. Kain, N. Yussouf, D. C. Dowell, D. M. Wheatley, K. H. Knopfmeier, and T. A. Jones, 2018: Advancing from convection-allowing NWP to Warn-on-Forecast: Evidence of progress. *Wea. Forecasting*, **33**, 599–607, https://doi.org/10.1175/WAF-D-17-0145.1.

Letkewicz, C. E., A. J. French, and M. D. Parker, 2013: Base-state substitution: An idealized modeling technique for approximating environmental variability. *Mon. Wea. Rev.*, **141**, 3062–3086, https://doi.org/10.1175/MWR-D-12-00200.1.

Lilly, D. K., 1982: The development and maintenance of rotation in convective storms. *Intense Atmospheric Vortices*, L. Bengtsson, Ed., Springer, 149–160.

——, 1986: The structure, energetics and propagation of rotating convective storms. Part II: Helicity and storm stabilization. *J. Atmos. Sci.*, **43**, 126–140, https://doi.org/10.1175/1520-0469(1986)043<0126:TSEAPO>2.0.CO;2.

Maddox, R. A., 1976: An evaluation of tornado proximity wind and stability data. *Mon. Wea. Rev.*, **104**, 133–142, https://doi.org/10.1175/1520-0493(1976)104<0133:AEOTPW>2.0.CO;2.

Markowski, P. M., and Y. P. Richardson, 2010: *Mesoscale Meteorology in Midlatitudes.* Wiley, 430 pp.

——, and ——, 2014: The influence of environmental low-level shear and cold pools on tornadogenesis: Insights from idealized simulations. *J. Atmos. Sci.*, **71**, 243–275, https://doi.org/10.1175/JAS-D-13-0159.1.

——, J. M. Straka, and E. N. Rasmussen, 2002: Direct surface thermodynamic observations within the rear-flank downdrafts of nontornadic and tornadic supercells. *Mon. Wea. Rev.*, **130**, 1692–1721, https://doi.org/10.1175/1520-0493(2002)130<1692:DSTOWT>2.0.CO;2.

——, Y. P. Richardson, M. Majcen, J. Marquis, and J. Wurman, 2011: Characteristics of the wind field in three nontornadic low-level mesocyclones observed by the Doppler on wheels radars. *Electron. J. Severe Storms Meteor.*, **6** (3), https://www.ejssm.org/ojs/index.php/ejssm/article/viewArticle/75.

Newton, C. W., and S. Katz, 1958: Movement of large convective rainstorms in relation to winds aloft. *Bull. Amer. Meteor. Soc.*, **39**, 129–136, https://doi.org/10.1175/1520-0477-39.3.129.

Parker, M. D., 2014: Composite VORTEX2 supercell environments from near-storm soundings. *Mon. Wea. Rev.*, **142**, 508–529, https://doi.org/10.1175/MWR-D-13-00167.1.

Peters, J. M., C. J. Nowotarski, and H. Morrison, 2019: The role of vertical wind shear in modulating maximum supercell updraft velocities. *J. Atmos. Sci.*, **76**, 3169–3189, https://doi.org/10.1175/JAS-D-19-0096.1.

——, ——, J. P. Mulholland, and R. L. Thompson, 2020: The influences of effective inflow layer streamwise vorticity and storm-relative flow on supercell updraft properties. *J. Atmos. Sci.*, **77**, 3033–3057, https://doi.org/10.1175/JAS-D-19-0355.1.

Rasmussen, E. N., 2003: Refined supercell and tornado forecast parameters. *Wea. Forecasting*, **18**, 530–535, https://doi.org/10.1175/1520-0434(2003)18<530:RSATFP>2.0.CO;2.

——, and D. O. Blanchard, 1998: A baseline climatology of sounding-derived supercell and tornado forecast parameters. *Wea. Forecasting*, **13**, 1148–1164, https://doi.org/10.1175/1520-0434(1998)013<1148:ABCOSD>2.0.CO;2.

Richardson, Y. P., K. K. Droegemeier, and R. P. Davies-Jones, 2007: The influence of horizontal environmental variability on numerically simulated convective storms. Part I: Variations in vertical shear. *Mon. Wea. Rev.*, **135**, 3429–3455, https://doi.org/10.1175/MWR3463.1.

Rotunno, R., and J. B. Klemp, 1982: The influence of the shear-induced pressure gradient on thunderstorm motion. *Mon. Wea. Rev.*, **110**, 136–151, https://doi.org/10.1175/1520-0493(1982)110<0136:TIOTSI>2.0.CO;2.

——, and J. Klemp, 1985: On the rotation and propagation of simulated supercell thunderstorms. *J. Atmos. Sci.*, **42**, 271–292, https://doi.org/10.1175/1520-0469(1985)042<0271:OTRAPO>2.0.CO;2.

Stensrud, D. J., and Coauthors, 2009: Convective-scale Warn-on-Forecast system. *Bull. Amer. Meteor. Soc.*, **90**, 1487–1500, https://doi.org/10.1175/2009BAMS2795.1.

Thompson, R. L., R. Edwards, J. A. Hart, K. L. Elmore, and P. Markowski, 2003: Close proximity soundings within supercell environments obtained from the Rapid Update Cycle. *Wea. Forecasting*, **18**, 1243–1261, https://doi.org/10.1175/1520-0434(2003)018<1243:CPSWSE>2.0.CO;2.

Wade, A. R., M. C. Coniglio, and C. L. Ziegler, 2018: Comparison of near- and far-field supercell inflow environments using radiosonde observations. *Mon. Wea. Rev.*, **146**, 2403–2415, https://doi.org/10.1175/MWR-D-17-0276.1.

Weisman, M. L., and J. B. Klemp, 1982: The dependence of numerically simulated convective storms on vertical wind shear and buoyancy. *Mon. Wea. Rev.*, **110**, 504–520, https://doi.org/10.1175/1520-0493(1982)110<0504:TDONSC>2.0.CO;2.

——, and ——, 1984: The structure and classification of numerically simulated convective stormsin directionally varying wind shears. *Mon. Wea. Rev.*, **112**, 2479–2498, https://doi.org/10.1175/1520-0493(1984)112<2479:TSACON>2.0.CO;2.

——, and R. Rotunno, 2000: The use of vertical wind shear versus helicity in interpreting supercell dynamics. *J. Atmos. Sci.*, **57**, 1452–1472, https://doi.org/10.1175/1520-0469(2000)057<1452:TUOVWS>2.0.CO;2.

Zeitler, J. W., and M. J. Bunkers, 2005: Operational forecasting of supercell motion: Review and case studies using multiple datasets. *Natl. Wea. Dig.*, **29**, 81–97.

Ziegler, C. L., E. R. Mansell, J. M. Straka, D. R. MacGorman, and D. W. Burgess, 2010: The impact of spatial variations of low-level stability on the life cycle of a simulated supercell storm. *Mon. Wea. Rev.*, **138**, 1738–1766, https://doi.org/10.1175/2009MWR3010.1.